

MRF-PINN: A Multi-Receptive-Field convolutional physics-informed neural network for solving partial differential equations

Shihong Zhang^a Chi Zhang^a Bosen Wang^{a,*}

^a *National Key Laboratory of Science and Technology on Aero-Engine Aero-thermodynamics,
Research Institute of Aero-Engine, Beihang University, Beijing 100191, China*

Abstract

Physics-informed neural networks (PINN) can achieve lower development and solving cost than traditional partial differential equation (PDE) solvers in scenarios such as reconstructing the physics field and solving the inverse problem. Therefore, in recent years, PINN has become a research highlight in the cross-field of deep learning and PDE solving. Due to the advantages of parameter sharing, spatial feature extraction and low inference cost, convolutional neural networks (CNN) are increasingly used in PINN. However, there are few studies on the general convolutional PINN model. To adapt convolutional PINN to different equations, researchers have to spend much time tuning critical hyperparameters. Furthermore, the effects of finite difference accuracy, model complexity, and mesh resolution on the prediction result of convolutional PINN are unclear. To fill the above research gaps, in this paper, (1) A Multi-Receptive-Field PINN (MRF-PINN) model is constructed to adapt different equation types and mesh resolutions without manual tuning. (2) The Taylor polynomial is used to pad the virtual nodes of the boundary. Based on this, the PDE loss is calculated using high-order finite difference, which improves the prediction accuracy and maintains the robustness of the solving process. (3) The generality and advantages of the MRF-PINN are verified in three typical linear PDEs (elliptic, parabolic, hyperbolic) and nonlinear PDEs (Navier-Stokes equations). (4)

* Corresponding author at: National Key Laboratory of Science and Technology on Aero-Engine Aero-thermodynamics, Research Institute of Aero-Engine, Beihang University, Beijing 100191, China
E-mail address: wangbosen@buaa.edu.cn (B.S. Wang).

The contribution of each receptive field to the final MRF-PINN result is analyzed, and the influence of finite difference accuracy, model complexity (channel number) and mesh resolution on the MRF-PINN result is tested. This paper shows that MRF-PINN can adapt to completely different equation types and mesh resolutions without any hyperparameter tuning. Further, the solving error is significantly decreased under high-order finite difference, large channel number, and high mesh resolution, which is expected to become a general convolutional PINN scheme.

Keywords: Physics-informed neural networks (PINN), Convolutional neural network (CNN), Multiple receptive fields, High-order finite difference, High resolution

1. Introduction

The traditional partial differential equation (PDE) solvers based on numerical discretization have vigorously developed in recent decades. They can be applied to industrial scenarios such as fluid mechanics[1], solid mechanics[2], heat transfer[3], and electromagnetism[4]. The traditional PDE numerical solving methods mainly include finite difference[5], finite element[6], finite volume[7], Lattice Boltzmann[8], smooth particle method[9] and so on. However, these PDE solving methods are challenging to integrate available fidelity data to improve solving accuracy and efficiency, and it also requires much iteration cost to solve the inverse problem[10]. In recent years, the development of physics-informed neural networks (PINN) has made up for the above shortcomings. In addition, PINN eliminates the dependence on large dataset under the constraint of prior physical knowledge, so it has become a new interesting method for PDE solving[11][12][13][14][15]. The neural network architectures used mainly by PINN are multilayer perceptron (MLP) and convolutional neural network (CNN). Beneficial from the advantages of parameter sharing, spatial feature extraction, and lightweight, CNN is used to construct PINN by more and more researchers[16][17][18]. However, the research on convolutional PINN is still relatively preliminary, especially in terms of model architecture[19], finite difference accuracy[16], weight estimation[20]. There is still huge room for

improvement in the convergence speed and solving accuracy in solving forward and inverse problems[14].

Researchers are committed to improving the efficiency, accuracy, and generality of PINN in solving forward and inverse problems from series aspects. In terms of model architecture, various architectures such as ResNet, U-Net, and Fourier neural operator are used to build PINN models[19][21][22], which can inhibit model degradation, adapt to image-to-image prediction, and accelerate the solving process. In terms of activation function, Jagtap proposed to apply the adaptive activation function with parameters to PINN, which can accelerate the convergence speed and reduce the prediction error[23]. In terms of multi-fidelity data integration, Meng used a composite PINN network to improve model accuracy while reducing dependence on high-cost high-fidelity data[24]. In terms of computational domain transformation, Gao transformed the irregular complex domain into the regular rectangular domain through coordinate transformation, enabling CNN to implement deployment and gradient computations under complex geometric conditions[25]. In terms of sampling method and physical constraint, LuLu used residual-based adaptive refinement, gradient-enhanced to reduce the number of sampling points, speed up the model training process, and reduce the solving error[26]. In terms of weight estimation, Wang proposed a dynamic weight estimation method to balance multiple loss functions in PINN networks[20]. In terms of optimization methods, researchers usually use Adam to optimize the model and then use L-BFGS-B to fine-tune the model as needed to improve the prediction accuracy[13].

The above improvement method greatly improves the generality and solving accuracy of PINN. However, in convolutional PINN, systematic research on the general network model, finite difference accuracy, model complexity, and mesh resolution is still relatively preliminary. This will be unfavorable for the CNN to play the advantages of efficient feature extraction and lightweight inference in PINN. Therefore, this paper designs a convolutional PINN model with multiple receptive fields (MRF-PINN). MRF-PINN can adapt to different equation types without manual

tuning, which is expected to be used as a general convolutional PINN design idea. Compared with the traditional fixed receptive field PINN, the advantages of MRF-PINN are verified experimentally. Finally, the effects of high-order finite difference, model complexity, and mesh resolution on the MRF-PINN prediction result are systematically studied.

This paper will describe the algorithm research on MRF-PINN in the following sections: In section 2, the algorithm we designed is described, including the MRF-PINN model, boundary padding, higher-order finite difference, loss function, and weight estimation method. In section 3, the method details and the results in solving three linear PDEs (elliptic, parabolic, hyperbolic) and nonlinear PDEs (Navier-Stokes equations) via PINN, FEM, and FVM are presented. In section 4, we compare the traditional fixed receptive field PINN to verify the advantage of MRF-PINN. Moreover, compared with the dynamic weight method, the dimension balance method proposed in this paper solves the Navier-Stokes equations more effectively. Section 5 tests the contribution of each receptive field to the final MRF-PINN result. The influence of finite difference accuracy, model complexity, and mesh resolution on the MRF-PINN result are tested systematically.

2. Methodology

This section will describe the MRF-PINN algorithm, including the MRF-PINN model, boundary padding and high-order finite difference, loss function, and weight estimation methods. As shown in Fig. 1, the solving process of the MRF-PINN is shown as follows:

MRF-PINN algorithm

- (a) Obtain initialized fields from boundary conditions using mean filtering.
 - (b) Estimate the loss weights of the PDE loss, boundary condition loss, initial condition loss, and data loss through manual tuning or the dimensional balance
-

method: $\lambda_{\text{PDEs}}, \lambda_{\text{BC}}, \lambda_{\text{IC}}, \lambda_{\text{data}}$.

for epoch=1, 2, 3, ..., epoch_{Adam} **do**

(c) Input the initialized fields into six encoder-decoder pairs to obtain the corresponding six physical fields. Each encoder-decoder's convolution kernels have different receptive fields. The parameters θ_1 of all encoder-decoder pairs need to be learned.

(d) The six intermediate physics fields output by encoder-decoders are recombined, and the same components are placed together.

(e) The final MRF-PINN result is obtained by linearly superimposing the recombined physical fields, and the parameters θ_2 of linear superimposition need to be learned.

(f) The MSE loss of the PDEs is calculated using the finite difference convolution operator as the equation loss L_{PDEs} .

(g) The MSE loss between the MRF-PINN result and the boundary conditions or initial conditions is calculated as the boundary condition loss L_{BC} and the initial condition loss L_{IC} .

(h) The MSE loss between the MRF-PINN result and the known data is calculated as data loss L_{data} .

(i) $L_{\text{PDEs}}, L_{\text{BC}}, L_{\text{IC}}, L_{\text{data}}$ are summed with weights $\lambda_{\text{PDEs}}, \lambda_{\text{BC}}, \lambda_{\text{IC}}, \lambda_{\text{data}}$ as the total loss L .

(j) The parameters of the encoder-decoder pairs θ_1 and the linear superposition θ_2 are optimized using the back-propagation algorithm and the Adam optimization algorithm, with a learning rate of 1e-4.

end

for epoch=1, ..., epoch_{L-BFGS} **do**

(k) The same steps as (c)~(i).

(l) The parameters of the encoder-decoder pairs θ_1 and the linear superposition θ_2 are fine-tuned using the back-propagation algorithm and the L-BFGS optimization

algorithm.

end

(m) Output the final MRF-PINN result.

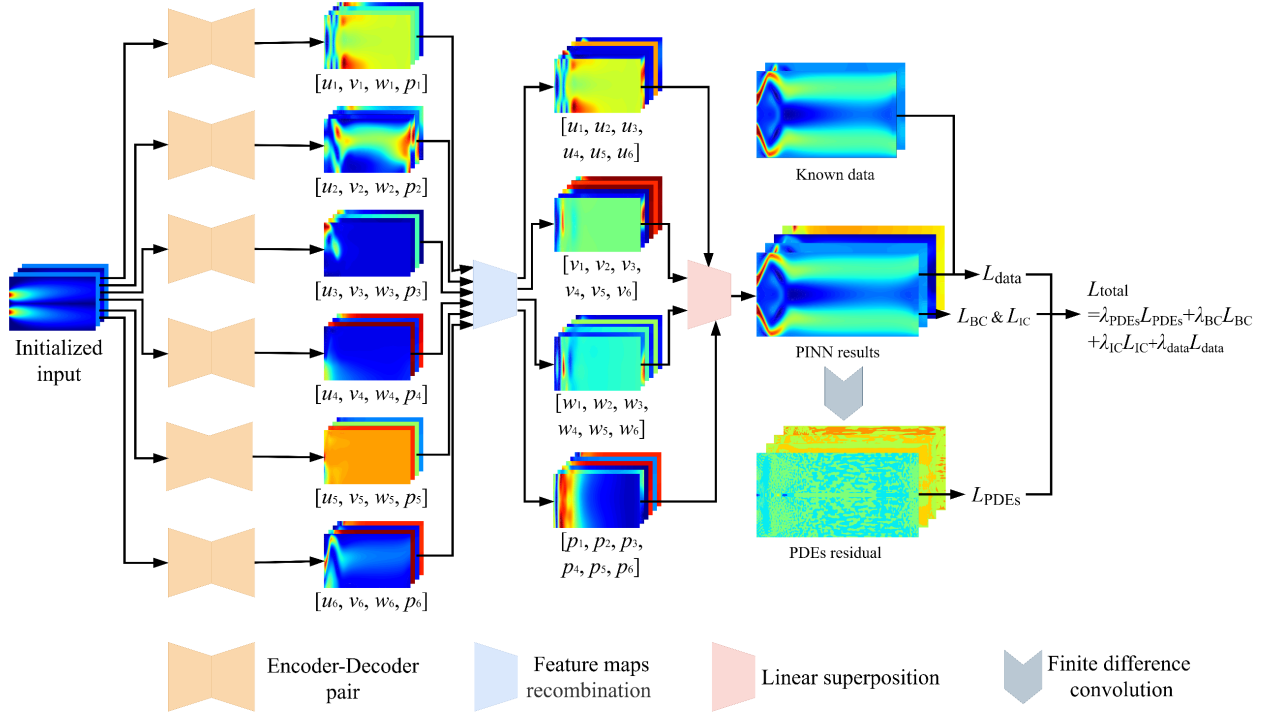


Fig. 1. MRF-PINN Model

2.1 MRF-PINN model

For convolutional PINN, if the mesh resolution of the input and output changes, the receptive field of the convolution kernel relative to the physics will also change simultaneously. For example, increasing the mesh resolution when solving the Navier-Stokes equations, the flow field structure (or vortex) will be described by more mesh elements. If the size of the convolution kernel remains unchanged, its receptive field will be reduced relative to the flow field structure. This will lead to (1) Hyperparameters such as the optimal receptive field need to be determined through repeated manual tuning. (2) At different mesh resolutions, the model's generalization will be weakened because the receptive field of the convolution kernel relative to the physical field has significantly changed, and the nonlinear mapping relationship

between input and output is seriously invalid. Therefore, as shown in Fig. 2, this paper constructs a resolution-adapted multiple receptive field dilated convolution. Based on that, the Encoder-Decoder pair is built as shown in Fig. 3.

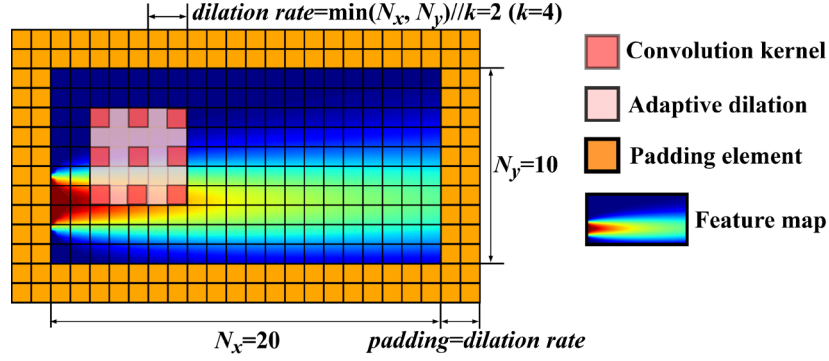


Fig. 2. Resolution-adapted dilated convolution, The size of the receptive field is determined by the dilation rate of the convolution kernel (The receptive field of 3×3 is padded to 5×5 with dilation rate=2), and the dilation rate of the convolution kernel is set to a fixed multiple of the input resolution (the multiple in the figure is 1/4).

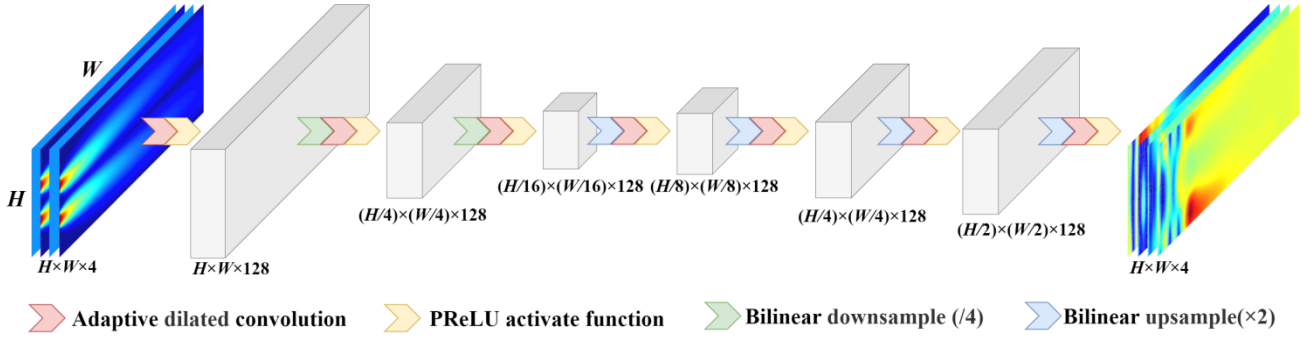


Fig. 3. Single Encoder-Decoder pair

In the dilated convolution with multiple receptive fields, the dilation rate of the convolution kernel and padding number of the feature map depend on current feature map size. For example, in one layer of the Encoder-Decoder pair, the size of feature map is $c \times h \times w$, which means that the input feature map has c channels, and the size of each channel is $h \times w$. The dilated rate of the convolution kernel of this layer and the padding number of the feature map are adaptive to $\max(\lfloor \min(h, w) / k \rfloor, 1)$, and

the k of the six Encoder-Decoder pairs are set to 2, 4, 8, 16, 32, 64, respectively. In this way, when each Encoder-Decoder propagates forward, the receptive field of each convolution kernel remains unchanged relative to its feature map, which is always $2 \times \max(\lfloor \min(h, w)/k \rfloor, 1) + 1$. The receptive fields of different Encoder-Decoder pairs are different, and the receptive fields of the six Encoder-Decoder pairs decrease relative to the feature maps. Finally, the outputs of the six Encoder-Decoder pairs are superposed linearly as the final prediction result of MRF-PINN:

$$u_i = \text{Encoder-Decoder}_i(u_{initial}) \quad i = 1, 2, 3, 4, 5, 6 \quad (1)$$

$$u_{PINN} = \sum_{i=1}^6 \theta_i \cdot u_i = \sum_{i=1}^6 \theta_i \cdot \text{Encoder-Decoder}_i(u_{initial}) \quad (2)$$

2.2 Boundary padding and high-order finite difference

Convolutional PINN performs finite difference through a fixed-parameter convolution kernel, and the accuracy of the finite difference directly determines the precision of the derivative.

Before performing finite-difference convolution, the PINN result should be reasonably boundary padded or one-sided difference near the boundary. In this paper, Taylor polynomial fitting is used to pad the boundary, which can ensure the finite difference accuracy near the boundary and simplify the finite difference algorithm.

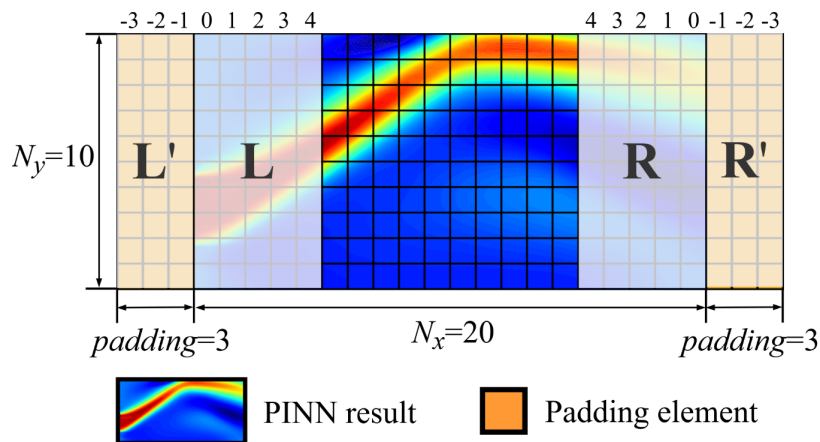


Fig. 4. Boundary padding before finite difference convolution

As shown as Fig. 4, before performing the sixth-order central difference in the x -direction, the left and right boundaries must be padded first. Assume that the variable u and its first three partial derivatives at n ($n=-3, -2, -1, 0, 1, 2, 3$) units away from the boundary of PINN result are $u^{(n)}, u_x^{(n)}, u_{xx}^{(n)}, u_{xxx}^{(n)}$, respectively. According to Taylor expansion:

$$u^{(n)} = u^{(0)} + n \cdot u_x^{(0)} + \frac{n^2}{2} \cdot u_{xx}^{(0)} + \frac{n^3}{6} \cdot u_{xxx}^{(0)} + o(n^3) \quad n = -3, -2, -1, 0, 1, 2, 3 \quad (3)$$

$$\begin{bmatrix} u^{(1)} - u^{(0)} \\ u^{(2)} - u^{(0)} \\ u^{(3)} - u^{(0)} \end{bmatrix} = \begin{bmatrix} 1 & 1/2 & 1/6 \\ 1 & 4/2 & 8/6 \\ 1 & 9/2 & 27/6 \end{bmatrix} \begin{bmatrix} u_x^{(0)} \\ u_{xx}^{(0)} \\ u_{xxx}^{(0)} \end{bmatrix} + o(n^3) \quad (4)$$

Similarly, for the padded virtual units, we have:

$$\begin{bmatrix} u^{(-1)} - u^{(0)} \\ u^{(-2)} - u^{(0)} \\ u^{(-3)} - u^{(0)} \end{bmatrix} = \begin{bmatrix} -1 & 1/2 & -\frac{1}{6} \\ -1 & 4/2 & -\frac{8}{6} \\ -1 & 9/2 & -\frac{27}{6} \end{bmatrix} \begin{bmatrix} u_x^{(0)} \\ u_{xx}^{(0)} \\ u_{xxx}^{(0)} \end{bmatrix} + o(n^3) \quad (5)$$

The values of the padded virtual units are:

$$\begin{bmatrix} u^{(-1)} \\ u^{(-2)} \\ u^{(-3)} \end{bmatrix} \approx \begin{bmatrix} u^{(0)} \\ u^{(0)} \\ u^{(0)} \end{bmatrix} + \begin{bmatrix} -1 & 1/2 & -\frac{1}{6} \\ -2 & 4/2 & -\frac{8}{6} \\ -3 & 9/2 & -\frac{27}{6} \end{bmatrix} \begin{bmatrix} 1 & 1/2 & 1/6 \\ 2 & 4/2 & 8/6 \\ 3 & 9/2 & 27/6 \end{bmatrix}^{-1} \begin{bmatrix} u^{(1)} - u^{(0)} \\ u^{(2)} - u^{(0)} \\ u^{(3)} - u^{(0)} \end{bmatrix} \quad (6)$$

In most cases, the distribution of physical variable u near the boundary is relatively smooth, and the size of the finite difference operator is generally much smaller than the total number of elements in the derivation direction. Therefore, it can also be assumed that in the derivation direction near the boundary, the distribution of physical variable u is a smooth cubic distribution (or quadratic distribution), that is:

$$u^{(n)} \equiv u^{(0)} + n \cdot u_x^{(0)} + \frac{n^2}{2} \cdot u_{xx}^{(0)} + \frac{n^3}{6} \cdot u_{xxx}^{(0)} \quad n = -3, -2, -1, 0, 1, 2, 3 \quad (7)$$

Obviously, this method is consistent with the results obtained by third-order Taylor expansion. Therefore, the Taylor expansion method or the undetermined coefficient method can be used to determine the value of the padded virtual element. In order to avoid being affected by some outliers, more internal nodes can be used to determine the value of the padded virtual node. But the equation is over-determined now, and the pseudo-inverse can be used instead of the original inverse:

$$\begin{bmatrix} u^{(-1)} \\ u^{(-2)} \\ u^{(-3)} \end{bmatrix} \approx \begin{bmatrix} u^{(0)} \\ u^{(0)} \\ u^{(0)} \end{bmatrix} + \begin{bmatrix} -1 & 1/2 & -\frac{1}{6} \\ -2 & 4/2 & -\frac{8}{6} \\ -3 & 9/2 & -\frac{27}{6} \end{bmatrix} \begin{bmatrix} 1 & 1/2 & 1/6 \\ 2 & 4/2 & 8/6 \\ 3 & 9/2 & 27/6 \\ \dots & \dots & \dots \end{bmatrix}^+ \begin{bmatrix} u^{(1)} - u^{(0)} \\ u^{(2)} - u^{(0)} \\ u^{(3)} - u^{(0)} \\ \dots \end{bmatrix} \quad (8)$$

After boundary padding, finite difference convolution is performed to calculate the PDE loss. Taking the six-order central difference as an example, its finite difference convolution is shown in Fig. 5. Before the finite differential convolution, the PINN result is padded in the derivation direction. The number of padded virtual units is half of the central difference order, which ensures that the size of the PINN result and the derivative result after central difference convolution remain unchanged. This paper adopts 2-order Taylor polynomials for boundary padding to robustly preserve the accuracy of derivatives on the boundary (since the highest order of PDE is 2). Then the finite difference convolution kernel with fixed parameters is used to act on the PINN result after boundary padding to obtain the derivative value of the physical field. The parameters of the convolution kernel when calculating the first and second derivatives are shown in Table 1:

Table 1

Parameters of the finite difference convolution kernel

Derivative order	Finite difference order	Parameters of the convolution kernel
1	2	$[-1/2, 0, 1/2]$
	4	$[1/12, -2/3, 0, 2/3, -1/12]$

	6	$[-1/60, 3/20, -3/4, 0, 3/4, -3/20, 1/60]$
	8	$[1/280, -4/105, 1/5, -4/5, 0, 4/5, -1/5, 4/105, -1/280]$
2	2	$[1, -2, 1]$
	4	$[-1/12, 4/3, -5/2, 4/3, -1/12]$
	6	$[1/90, -3/20, 3/2, -49/18, 3/2, -3/20, 1/90]$
	8	$[-1/560, 8/315, -1/5, 8/5, -205/72, 8/5, -1/5, 8/315, -1/560]$

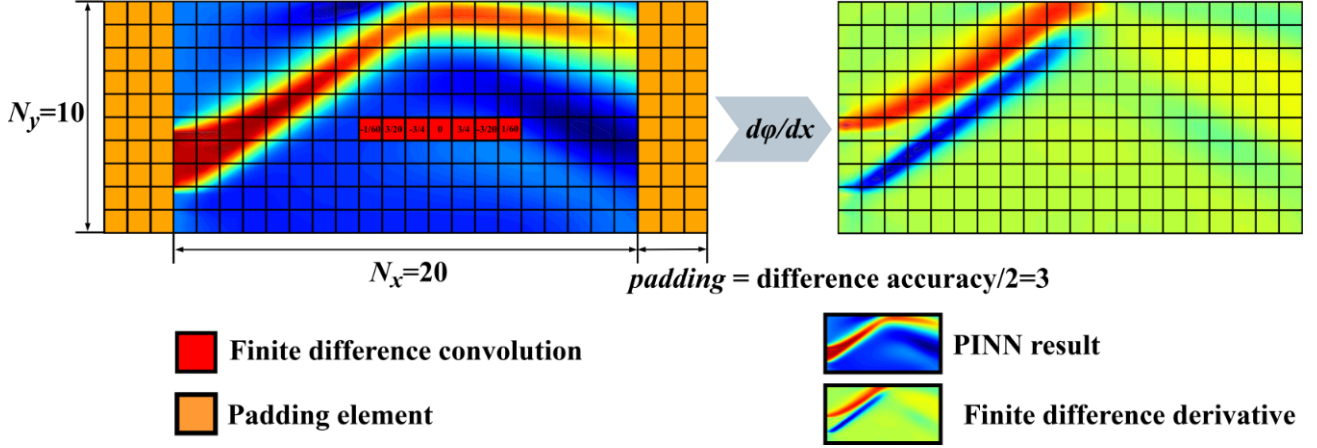


Fig. 5. Boundary padding and six-order finite difference convolution

2.3 Loss functions and weight estimation

For a PINN network $\hat{y} = \text{PINN}(x; \theta)$, its loss function consists of the following parts:

(1) PDE loss. Variables x and y should satisfy the PDE relationship $f(x, y, \frac{dy}{dx}, \frac{d^2y}{dx^2}, \dots) = 0$. Therefore, the PDE MSE loss is defined as

$$L_{PDEs} = \frac{1}{N_{\Omega}} \sum_i f^2 \left(x_i, y_i, \frac{dy_i}{dx_i}, \frac{d^2y_i}{dx_i^2}, \dots \right) \quad (9)$$

(2) Boundary condition loss, which is the MSE error between the predicted boundary value and the known boundary condition. Taking the Dirichlet boundary condition as an example, the boundary condition loss is defined as

$$L_{BC} = \frac{1}{N_{\partial\Omega}} \sum_i (\hat{y}_i - y_i)^2 \quad (10)$$

(3) Initial condition loss, which is the MSE error between the predicted value \hat{y}

at $t=0$ and the given initial condition. The MSE loss of the initial condition is defined as

$$L_{IC} = \frac{1}{N_{t=0}} \sum_i (\hat{y}_i - y_i)^2 \quad (11)$$

(4) Data loss, which is the MSE error between the PINN prediction \hat{y} and the known data. The MSE loss of the data is defined as

$$L_{data} = \frac{1}{N_{data}} \sum_i (\hat{y}_i - y_i)^2 \quad (12)$$

The total loss of PINN is the weighted sum of the above losses:

$$L = \lambda_{PDEs} L_{PDEs} + \lambda_{BC} L_{BC} + \lambda_{IC} L_{IC} + \lambda_{data} L_{data} \quad (13)$$

Now, the back-propagation algorithm can be used to optimize the parameters θ of PINN $\hat{y} = NN(x; \theta)$ until the loss meets the convergence requirements. The loss weights $[\lambda_{PDEs}, \lambda_{BC}, \lambda_{IC}, \lambda_{data}]$ directly determines the influence of each loss on the parameter optimization. Therefore, the loss weight will directly affect the solving efficiency and convergence of PINN.

In the current research, weight loss is usually determined by manual tuning or dynamic weight estimation. Besides, this paper proposes a dimensional balance method for the Navier-Stokes equations.

Manual tuning is a tedious and time-consuming task, which is only operable when the number of loss functions is few (for example, only PDE loss and boundary condition loss). In this paper, there are only PDE loss L_{PDEs} and boundary condition loss L_{BC} when solving the linear PDEs, so their loss weights are set manually.

The dynamic weight method utilizes the derivative information of each loss to the parameters, then balances the dependence on each part of the loss when parameters are updated. The dynamic weight method eliminates the blindness of human tuning, but it will increase the number of back-propagation, thereby reducing the optimization speed of the PINN. The dynamic weight method is performed by following steps:

(1) Back-propagation is performed for PDE loss L_{PDEs} , boundary condition loss,

initial condition loss L_{IC} , data loss L_{data} to obtain $\nabla_{\theta} L_{PDEs}$, $\nabla_{\theta} L_{BC}$, $\nabla_{\theta} L_{IC}$, $\nabla_{\theta} L_{data}$ and $|\nabla_{\theta} L_{PDEs}|$, $|\nabla_{\theta} L_{BC}|$, $|\nabla_{\theta} L_{IC}|$, $|\nabla_{\theta} L_{data}|$.

(2) Calculate the new loss weights:

$$\hat{\lambda}_{PDEs}^{(k+1)} = 1 \quad (14)$$

$$\hat{\lambda}_{BC}^{(k+1)} = \frac{|\nabla_{\theta} L_{PDEs}|}{|\nabla_{\theta} L_{BC}|} \quad (15)$$

$$\hat{\lambda}_{IC}^{(k+1)} = \frac{|\nabla_{\theta} L_{PDEs}|}{|\nabla_{\theta} L_{IC}|} \quad (16)$$

$$\hat{\lambda}_{data}^{(k+1)} = \frac{|\nabla_{\theta} L_{PDEs}|}{|\nabla_{\theta} L_{data}|} \quad (17)$$

(3) Update the loss weights, $\alpha=0.1$ is the update weight coefficient.

$$\lambda_{PDEs}^{(k+1)} = 1 \quad (18)$$

$$\lambda_{BC}^{(k+1)} = \alpha \hat{\lambda}_{BC}^{(k+1)} + (1 - \alpha) \lambda_{BC}^{(k)} \quad (19)$$

$$\lambda_{IC}^{(k+1)} = \alpha \hat{\lambda}_{IC}^{(k+1)} + (1 - \alpha) \lambda_{IC}^{(k)} \quad (20)$$

$$\lambda_{data}^{(k+1)} = \alpha \hat{\lambda}_{data}^{(k+1)} + (1 - \alpha) \lambda_{data}^{(k)} \quad (21)$$

This paper uses the dynamic weight method to assist in setting the loss weights in solving linear PDEs. However, the dynamic weight method has been verified invalid when solving the Navier-Stokes equations due to too many loss functions and the magnitude difference. However, the dimensions of the Navier-Stokes equations are easy to estimate, and the dimensional estimation method has been maturely applied to the study of fluids. Therefore, this paper determines the weights of the loss functions based on the idea of dimensional balance:

(1) Normalize the equation's variables to \tilde{x} , \tilde{y} , and \tilde{y} to separate the dimensions of each loss function:

$$L_{PDEs} = \frac{1}{N_{\Omega}} \sum_i f^2 \left(x_i, y_i, \frac{dy_i}{dx_i}, \frac{d^2 y_i}{dx_i^2}, \dots \right) = X^a Y^b \cdot \frac{1}{N_{\Omega}} \sum_i f^2 \left(\tilde{x}_i, \tilde{y}_i, \frac{d\tilde{y}_i}{d\tilde{x}_i}, \frac{d^2 \tilde{y}_i}{d\tilde{x}_i^2}, \dots \right) \quad (22)$$

$$L_{BC} = X^c Y^d \frac{1}{N_{\partial\Omega}} \sum_i (\tilde{y}_i - \tilde{y}_i)^2 \quad (23)$$

$$L_{IC} = X^e X^f \frac{1}{N_{t=0}} \sum_i (\tilde{y}_i - \tilde{y}_i)^2 \quad (24)$$

$$L_{data} = X^g X^h \frac{1}{N_{data}} \sum_i (\tilde{y}_i - \tilde{y}_i)^2 \quad (25)$$

(2) Perform dimensional balance (or normalization) for each loss function:

$$\tilde{L}_{PDEs} = X^{-a} Y^{-b} \cdot L_{PDEs} = \frac{1}{N_{\Omega}} \sum_i f^2 \left(\tilde{x}_i, \tilde{y}_i, \frac{d\tilde{y}_i}{d\tilde{x}_i}, \frac{d^2\tilde{y}_i}{d\tilde{x}_i^2}, \dots \right) \quad (26)$$

$$\tilde{L}_{BC} = X^{-c} Y^{-d} \cdot L_{BC} = \frac{1}{N_{\partial\Omega}} \sum_i (\tilde{y}_i - \tilde{y}_i)^2 \quad (27)$$

$$\tilde{L}_{IC} = X^{-e} X^{-f} \cdot L_{IC} = \frac{1}{N_{t=0}} \sum_i (\tilde{y}_i - \tilde{y}_i)^2 \quad (28)$$

$$\tilde{L}_{data} = X^{-g} X^{-h} \cdot L_{data} = \frac{1}{N_{data}} \sum_i (\tilde{y}_i - \tilde{y}_i)^2 \quad (29)$$

The total loss is defined as:

$$\begin{aligned} L &= \tilde{L}_{PDEs} + \tilde{L}_{BC} + \tilde{L}_{IC} + \tilde{L}_{data} \\ &= X^{-a} Y^{-b} \cdot L_{PDEs} + X^{-c} Y^{-d} \cdot L_{BC} + X^{-e} Y^{-f} \cdot L_{IC} + X^{-g} Y^{-h} \cdot L_{data} \end{aligned} \quad (30)$$

The loss weights are determined as:

$$\lambda_{PDEs} = X^{-a} Y^{-b} \quad (31)$$

$$\lambda_{BC} = X^{-c} Y^{-d} \quad (32)$$

$$\lambda_{IC} = X^{-e} Y^{-f} \quad (33)$$

$$\lambda_{data} = X^{-g} Y^{-h} \quad (34)$$

3. Numerical experiment

MRF-PINN, finite element method (FEM), and finite volume method (FVM) are used to solve three types of linear PDEs (elliptic, hyperbolic, parabolic) and nonlinear PDEs (Navier-Stokes equations). Based on the numerical experiments, the advantages and characteristics of MRF-PINN are further verified. To quantify the solve error of MRF-PINN, we define the two-norm error ε between MRF-PINN result and traditional numerical (FEM and FVM) result to measure the accuracy of PINN.

$$\varepsilon = \|u_{PINN} - u_{FEM}\|_2 / \|u_{FEM}\|_2 \quad (35)$$

$$\varepsilon = \|u_{PINN} - u_{FVM}\|_2 / \|u_{FVM}\|_2 \quad (36)$$

3.1 Linear PDEs

Second-order linear PDEs can describe a large number of physical phenomena succinctly, such as temperature fields, electromagnetic fields, gravitational fields, diffusion, and vibration. Second-order linear PDEs can be typically classified into elliptic, parabolic, and hyperbolic equations. The dependence and influence domains of these three kinds of equations are different, so they can describe various physical phenomena of equilibrium, approaching equilibrium, and non-equilibrium.

A general second-order linear PDE has the following form:

$$a \frac{\partial^2 u}{\partial x^2} + b \frac{\partial^2 u}{\partial x \partial y} + c \frac{\partial^2 u}{\partial y^2} + d \frac{\partial u}{\partial x} + e \frac{\partial u}{\partial y} + fu = g \quad (37)$$

Elliptic($b^2 - 4ac < 0$), parabolic($b^2 - 4ac = 0$), and hyperbolic($b^2 - 4ac > 0$) PDEs can be obtained by adjusting the coefficients of this equation. The PDE coefficients are set as shown in Table 2 and then PINN and FEM are used to solve the PDEs in three forms:

Table 2

Second-order linear PDE coefficients

PDE types	a	b	c	d	e	f	g
Elliptic	1	0	1	2	2	4	4
Parabolic	1	0	0	-2	-2	4	4
Hyperbolic	1	0	-1	0	0	0	0

The details of the MRF-PINN are: the mesh resolution of input and output is 32×64 . Input is the initial field mean filtered from the boundary to the center, n is the distance from the boundary to a row/column:

$$I(n+1) = I(n) \otimes [1/3 \quad 1/3 \quad 1/3] \quad n = 0, 1, 2, \dots, N_x (\text{or } N_y) \quad (38)$$

The receptive field sizes of the six Encoder-Decoder pairs are 33, 17, 9, 5, 3, and 3, respectively, which are obtained by dilating a 3×3 convolution kernel, and the relevant parameters are shown in Table 3. The padded virtual node is obtained by

fitting a second-order Taylor polynomial. The finite difference is the 8-order central difference. The loss function is the PDE loss and the boundary condition loss, and their weights are set to 1 and 1000. During the MRF-PINN solving process, the Adam optimizer is used to optimize 9000 epochs with a learning rate of $1e-4$. Then the L-BFGS optimizer is used to fine-tune MRF-PINN and run 500 epochs.

Table 3

Details of MRF-PINN dilated convolution for solving linear PDEs.

Enc-Dec	Enc-Dec -1	Enc-Dec- 2	Enc-Dec- 3	Enc-Dec- 4	Enc-Dec- 5	Enc-Dec- 6
k	2	4	8	16	32	64
Dilation rate	16	8	4	2	1	1
Padding	16	8	4	2	1	1
Receptive field	33	17	9	5	3	3
Receptive field/ $\min(h,w)$	$33/32 \approx 1.03$	$17/32 \approx 0.53$	$9/32 \approx 0.28$	$5/32 \approx 0.16$	$3/32 \approx 0.09$	$3/32 \approx 0.09$

The details of the FEM are: the mesh resolution is 200×400 , and the solver is MUMPS. In the MUMPS numerical solver, the equations and constraints are discretized on the elements to solve the linear equation $Ax=b$. MUMPS solves the inverse matrix of A to solve the PDE, and its realization method is Gaussian decomposition.

3.1.1 Elliptic PDE

The Ellipse PDEs are often used to describe physical phenomena in equilibrium, such as steady temperature field and steady potential distribution. The Elliptic PDEs do not have characteristic lines. Their dependence and influence domain covers the entire domain.

The elliptic PDE and its boundary conditions we solved are:

$$\begin{cases} \frac{\partial^2 u}{\partial x^2} + \frac{\partial^2 u}{\partial y^2} + 2\frac{\partial u}{\partial x} + 2\frac{\partial u}{\partial y} + 4u = 4 & 0 < x < 1, 0 < y < 2 \\ u|_{x=0} = -\sin(\pi y) & u|_{x=1} = \sin(\pi y) & 0 < y < 2 \\ u|_{y=0} = \sin(2\pi x) & u|_{y=2} = -\sin(2\pi x) & 0 < x < 1 \end{cases} \quad (39)$$

Fig. 6 compares the results using the MRF-PINN and FEM methods. Their results are very similar, with an error of 0.0127.

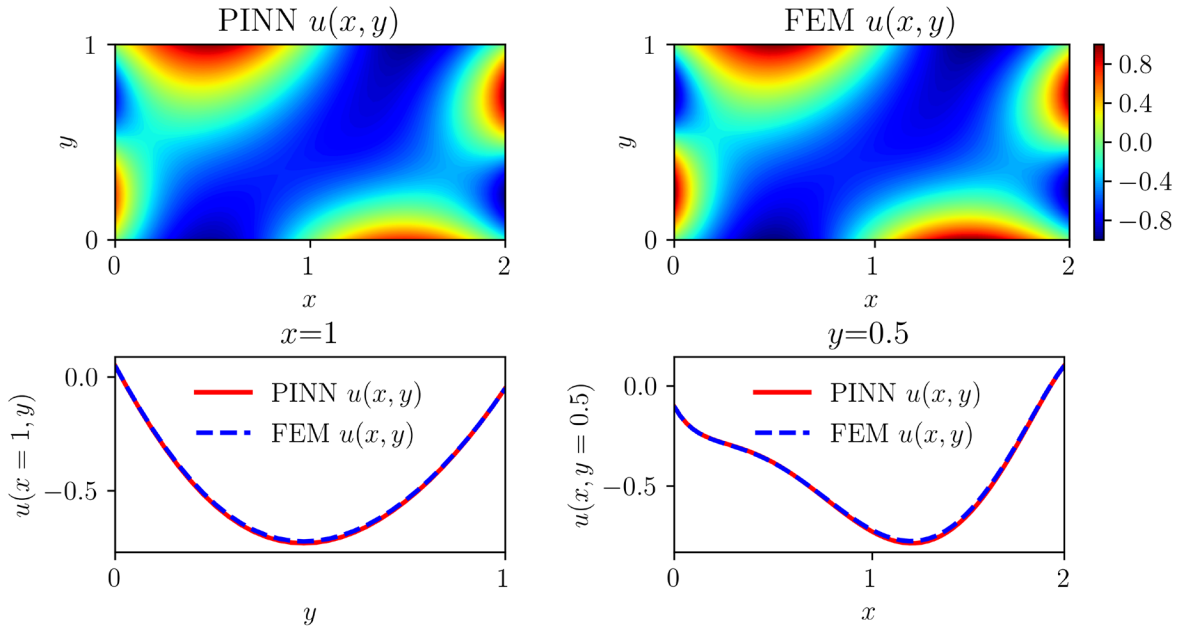


Fig. 6. Results of solving elliptic PDE by MRF-PINN and FEM method

3.1.2 Parabolic PDE

Parabolic PDEs are often used to describe physical processes that approach equilibrium, such as unsteady heat conduction and diffusion. The parabolic PDE has only one characteristic line, so one state only depends on the previous moment and affects the following moment. The parabolic PDE and its boundary conditions we solved are:

$$\begin{cases} \frac{\partial^2 u}{\partial x^2} - 2\frac{\partial u}{\partial x} - 2\frac{\partial u}{\partial y} + 4u = 4 & 0 < x < 1, 0 < y < 2 \\ u|_{x=0} = -\sin(\pi y) & u|_{x=1} = \sin(\pi y) & 0 < y < 2 \\ u|_{y=0} = \sin(2\pi x) & & 0 < x < 1 \end{cases} \quad (40)$$

Fig. 7 compares the results using the MRF-PINN and FEM methods. Their results are very similar, with an error of 0.00736.

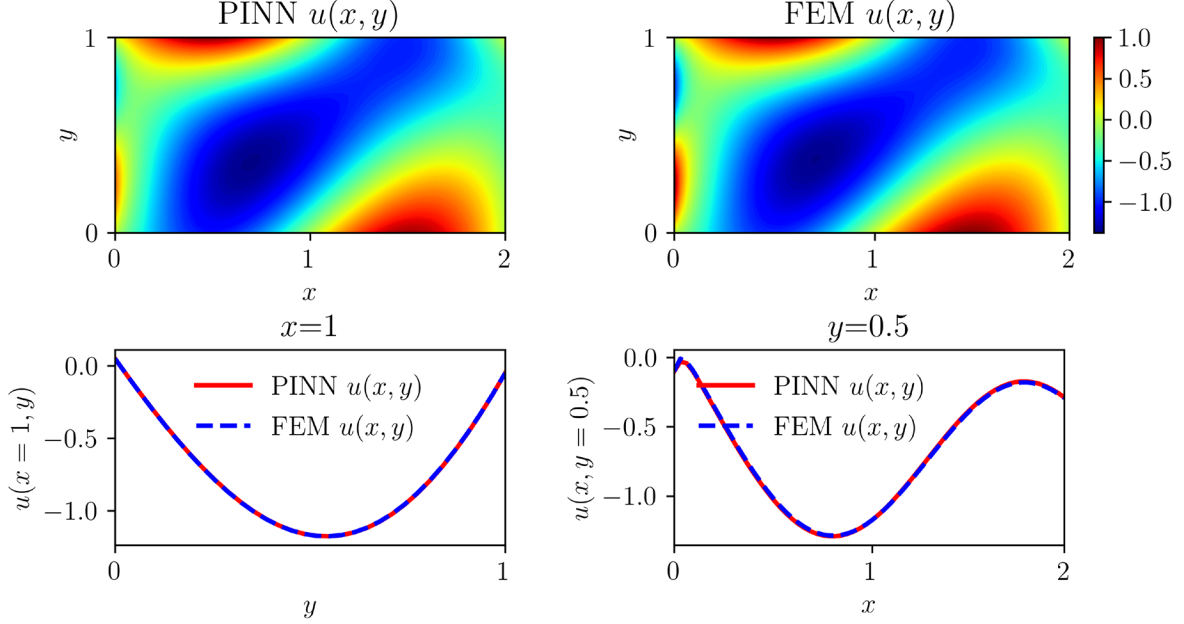


Fig. 7. Results of solving parabolic PDE by MRF-PINN and FEM method

3.1.3 Hyperbolic PDE

Hyperbolic PDEs are often used to describe non-equilibrium wave phenomena, such as mechanical, sound, and electromagnetic waves. The hyperbolic PDE has two characteristic lines, so the dependence and influence domain of one point in time and space is limited. The hyperbolic PDE and its boundary conditions we solved are:

$$\left\{ \begin{array}{ll} \frac{\partial^2 u}{\partial x^2} - \frac{\partial^2 u}{\partial y^2} = 0 & 0 < x < 1, 0 < y < 2 \\ u|_{x=0} = 0 & u|_{x=1} = 0 \quad 0 < y < 2 \\ u|_{y=0} = \sin(2\pi x) & u|_{y=2} = \sin(2\pi x) \quad 0 < x < 1 \end{array} \right. \quad (41)$$

Fig. 8 compares the results using the PINN and FEM methods. Their results are very similar, with an error of 0.05512.

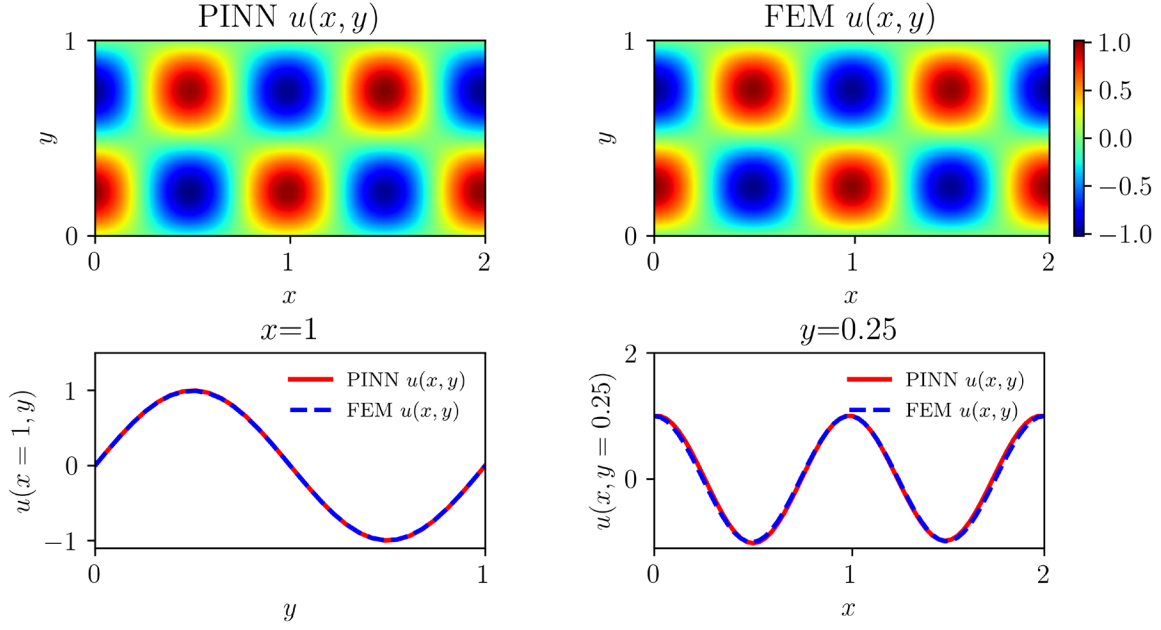


Fig. 8. Results of solving hyperbolic PDE by MRF-PINN and FEM method

3.2 Nonlinear PDEs: Navier-Stokes equations

The Navier-Stokes equations are the fundamental governing equations of fluid dynamics and are used to describe the mass, momentum, and energy of Newtonian fluid flow under the continuous assumption. The Navier-Stokes equations are tremendous nonlinear PDEs, so solving the Navier-Stokes equations can more effectively prove the validity of MRF-PINN.

The details of the MRF-PINN are: the mesh resolution of input and output is 128×1536 , Input is the initial field mean filtered from upstream to downstream, n is the distance from the upstream boundary to a row/column:

$$I(n+1) = I(n) \otimes \begin{bmatrix} 1/3 & 1/3 & 1/3 \end{bmatrix} \quad n = 0, 1, 2, \dots, N_x (\text{or } N_y) \quad (42)$$

The receptive field sizes of the six Encoder-Decoder pairs are 129, 65, 33, 17, 9, and 5, respectively, which are obtained by dilating a 3×3 convolution kernel, and the relevant parameters are shown in Table 4. The padded virtual node is obtained by fitting a second-order Taylor polynomial. The finite difference is the 8-order central difference. The loss function is the PDE loss, boundary condition loss, and data loss. The known data are two velocity components u and v , which parallel to the z - O - r

plane. The data that need to be inferred are the vertical velocity component w and the pressure p . In this way, we make up for the inability of the PIV experiment to measure the vertical velocity components and pressure. The loss weights are set to 16384 for mass and momentum PDEs in z, r, θ direction, 1 for boundary condition loss and data loss. During the MRF-PINN solving process, the Adam optimizer is used to optimize 30000 epochs with a learning rate of 1e-4. Then the L-BFGS optimizer is used to fine-tune MRF-PINN and run 1000 epochs.

Table 4

Details of MRF-PINN dilated convolution for solving Navier-Stokes PDEs

Enc-Dec	Enc-Dec-1	Enc-Dec-2	Enc-Dec-3	Enc-Dec-4	Enc-Dec-5	Enc-Dec-6
k	2	4	8	16	32	64
Dilation rate	64	32	16	8	4	2
Padding	64	32	16	8	4	2
Receptive field	129	65	33	17	9	5
Receptive field/min(h, w)	129/128 \approx 1.0	65/128 \approx 0.51	33/128 \approx 0.26	17/128 \approx 0.13	9/128 \approx 0.09	5/128 \approx 0.04

The details of the FVM are: the mesh resolution is 150×1800 , and the velocity-pressure coupling algorithm is adopted. The discretization method is second-order discretization for pressure and QUICK for momentum discretization.

The Navier-Stokes PDEs solved in this paper is axisymmetric swirl flow in two-dimensional cylindrical coordinate.

$$\left\{ \begin{array}{l} \frac{\partial u}{\partial z} + \frac{1}{r} \frac{\partial(rv)}{\partial r} = 0 \quad 0 < r < 1.5 \quad 0 < z < 18 \\ u \frac{\partial u}{\partial z} + v \frac{\partial u}{\partial r} = -\frac{1}{\rho} \frac{\partial p}{\partial x} + \nu \left(\frac{\partial^2 u}{\partial z^2} + \frac{\partial^2 u}{\partial r^2} + \frac{1}{r} \frac{\partial u}{\partial r} \right) \quad 0 < r < 1.5 \quad 0 < z < 18 \\ u \frac{\partial v}{\partial z} + v \frac{\partial v}{\partial r} - \frac{w^2}{r} = -\frac{1}{\rho} \frac{\partial p}{\partial r} + \nu \left(\frac{\partial^2 v}{\partial z^2} + \frac{\partial^2 v}{\partial r^2} + \frac{1}{r} \frac{\partial v}{\partial r} - \frac{v}{r^2} \right) \quad 0 < r < 1.5 \quad 0 < z < 18 \\ u \frac{\partial w}{\partial z} + v \frac{\partial w}{\partial r} - \frac{vw}{r} = \nu \left(\frac{\partial^2 w}{\partial z^2} + \frac{\partial^2 w}{\partial r^2} + \frac{1}{r} \frac{\partial w}{\partial r} - \frac{w}{r^2} \right) \quad 0 < r < 1.5 \quad 0 < z < 18 \\ v|_{r=0} = w|_{r=0} = 0, \quad \frac{\partial u}{\partial r} \Big|_{r=0} = 0 \quad u|_{r=1.5} = v|_{r=1.5} = w|_{r=1.5} = 0 \quad 0 < z < 18 \\ u|_{z=0} = w|_{z=0} = 5.88 \quad 0.3 < z < 0.7 \\ p|_{z=18} = 0 \\ u = v = w = 0 \quad \text{other BCs} \end{array} \right. \quad (43)$$

Fig. 9 and Fig. 10 show the results of solving the Navier-Stokes PDEs using MRF-PINN and FVM methods. The prediction results of the two methods are relatively similar, and the errors of velocity u , v , w , and pressure p are 0.0609, 0.0249, 0.0376, and 0.0522, respectively.

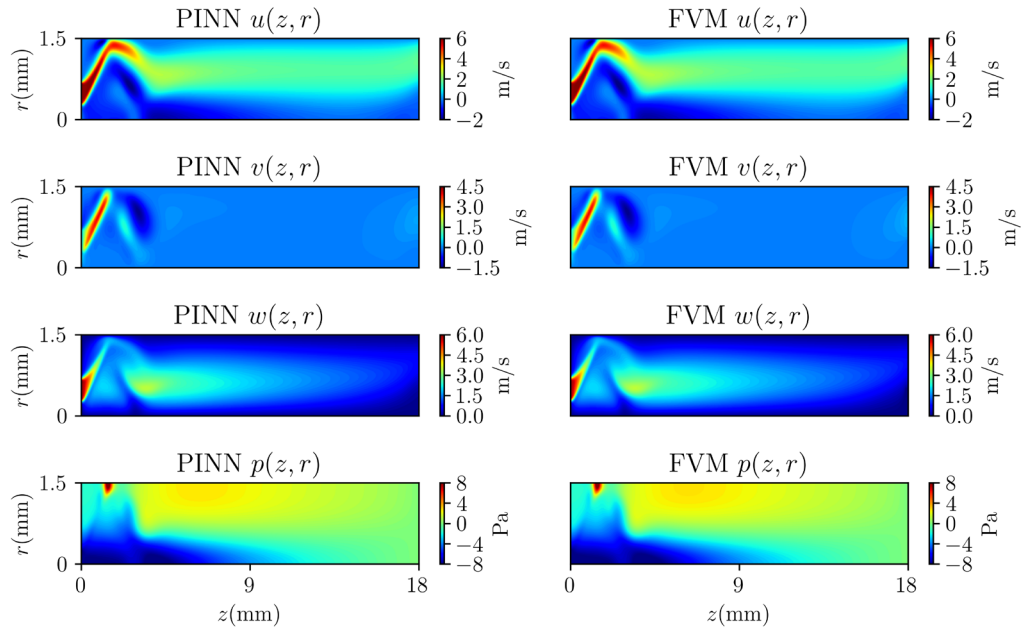


Fig. 9. Results of solving Navier-Stokes PDEs by MRF-PINN and FVM method

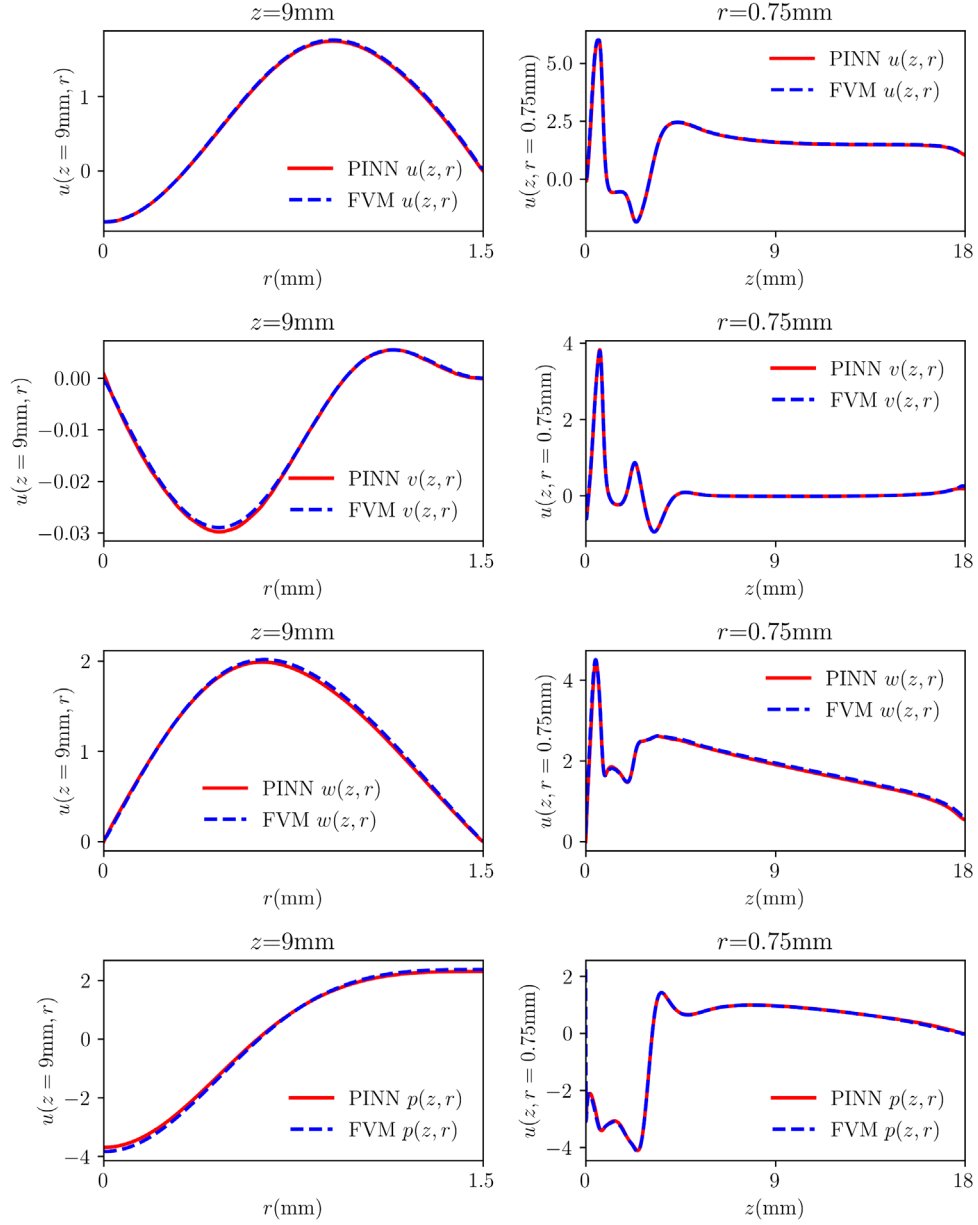


Fig. 10. Results of solving Navier-Stokes PDEs by MRF-PINN and FVM method

Based on the above MRF-PINN, FEM, and FVM algorithms, section 4 will verify the advantages of MRF-PINN and the dimensional balance method. Section 5 will discuss the influence of finite difference accuracy and mesh resolution on MRF-PINN results.

4. Algorithm advantages

4.1 MRF-PINN

This paper proposes the resolution-adapted MRF-PINN shown in section 2.1 to avoid time-consuming hyperparameter tuning. In order to quantify the contribution of Encoder-Decoder pairs with different receptive fields to the final MRF-PINN result, we define the correlation coefficient R to measure their similarity. If the R value approaches 1, the Encoder-Decoder output is more similar to the final MRF-PINN result. As the R value approaches 0, they are less similar.

$$R_i = \frac{|u_i \cdot u|}{\|u_i\|_2 \|u\|_2} \quad (44)$$

We test the R values between the Encoder-Decoder outputs and the final MRF-PINN results under different channel numbers. Fig. 11, Fig. 12, Fig. 13 and Fig. 14 show the R values under different PINN channels when solving the ellipse, parabola, hyperbolic, and Navier-Stokes PDEs, respectively. When solving the hyperbolic PDE, the R values between the Encoder-Decoder pair outputs with a larger receptive field(u_1, u_2) and the final MRF-PINN result(u) are very small, showing an obvious tendency to a small receptive field(u_3, u_4, u_5, u_6). When solving other PDEs, there is no strong regularity between R value, channel number, and receptive field, indicating that PINN does not show a strong tendency to a specific receptive field. Therefore, it is rare for convolutional PINN to tend to a specific receptive field stably. The generality of the PINN under different equations will be seriously weakened if the receptive field is set manually, and the tuning cost will significantly increase.

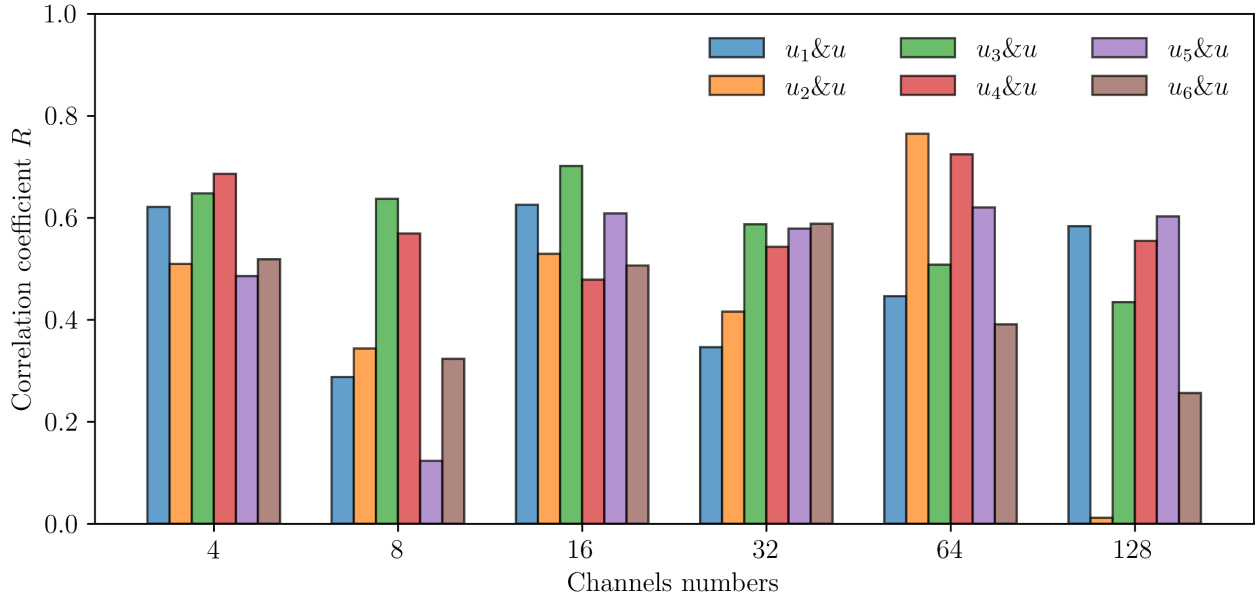


Fig. 11. Correlation coefficients(R) for elliptic equations. In most cases, the R values of different channel numbers and Encoder-Decoders have no apparent regularity. The output of Encoder-Decoder 2 u_2 is significantly suppressed only when the channel number is 128.

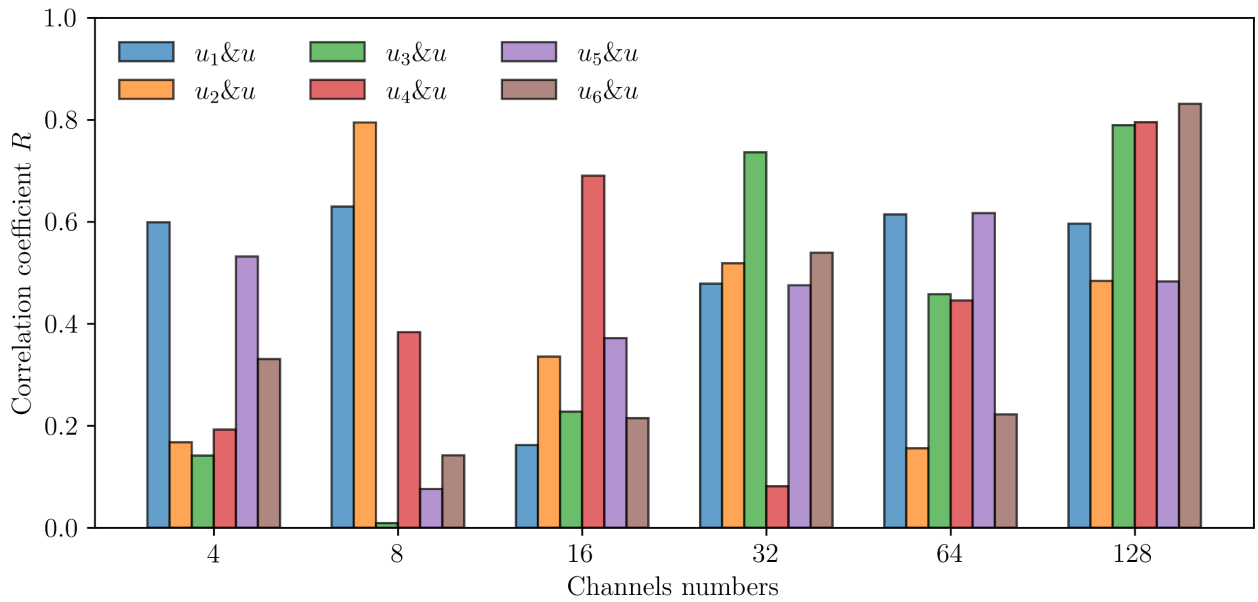


Fig. 12. Correlation coefficients(R) for parabolic equations. When the channel number increases, the R value of each Encoder-Decoder pair output improves, but the regularity is still weak.

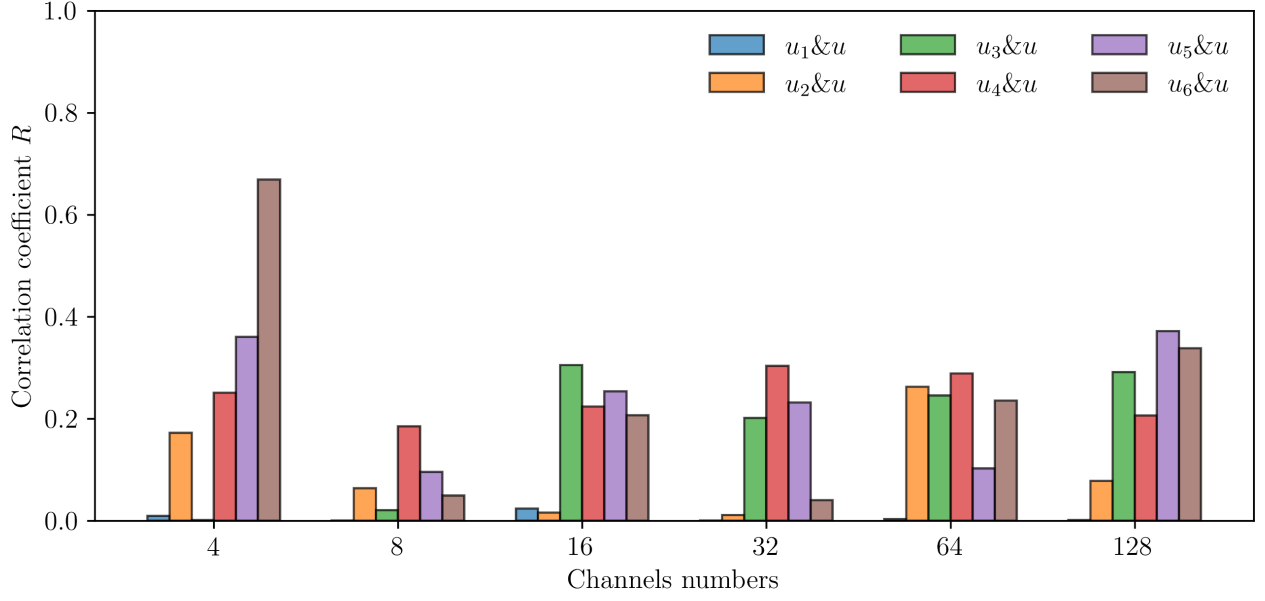


Fig. 13. Correlation coefficients(R) for hyperbolic equations. The Encoder-Decoder pairs tend to small receptive fields(u_3, u_4, u_5, u_6) and suppress the large receptive fields(u_1, u_2).

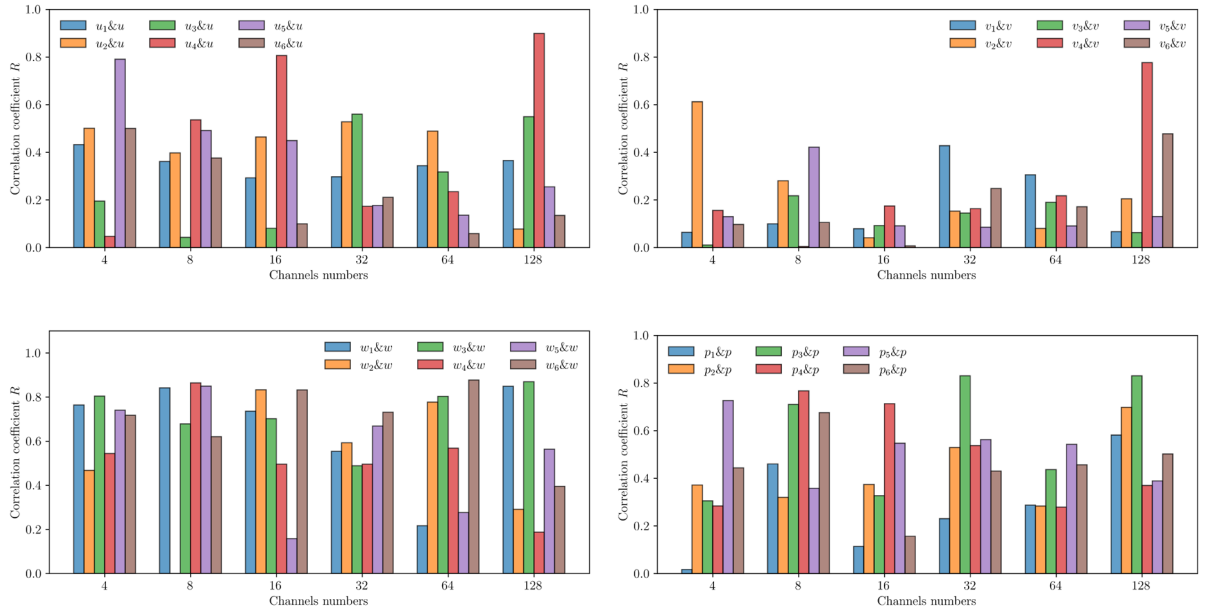


Fig. 14. Correlation coefficient(R) for the Navier-Stokes equations. The R values of different Encoder-Decoders have no significant regularity with the channel number.

In order to further prove the advantages of MRF-PINN over the fixed receptive field, we tested PINN with five fixed receptive fields(3, 5, 7, 9, and 11) and compared the solve error with MRF-PINN. The mesh resolution is 128×256 for Linear PDEs and 128×1536 for Navier-Stokes PDEs. As shown in Table 5, Table 6, Table 7, and Table 8, the optimal receptive fields for the ellipse, parabola, hyperbolic, and Navier-Stokes PDEs are 3, 7, 11, and 11, respectively. These optimal receptive fields require many times of manual tuning to achieve. However, the solving error of MRF-PINN is comparable to the optimal fixed receptive field in most cases. Compared with the optimal fixed receptive field PINN, the error of MRF-PINN in solving ellipse, parabolic and hyperbolic equations is 3.5% larger, 3.4% smaller, and 20% larger, respectively. For the nonlinear Navier-Stokes PDEs, the fitting error for u is 0.16% larger, the fitting error for v and the inference error for w and p are 9.1%, 1.5%, and 1.1% smaller, respectively. The comparison with the fixed receptive field PINN proves that the resolution-adapted MRF-PINN can reduce the tuning cost and suppress the resolving error well.

Table 5

Errors of solving elliptic PDE using fixed receptive field PINN and MRF-PINN

receptive field	3	5	7	9	11	MRF-PINN
error	0.00254	0.00528	0.00290	0.00290	0.00295	0.00263

Table 6

Errors of solving parabolic PDE using fixed receptive field PINN and MRF-PINN

receptive field	3	5	7	9	11	MRF-PINN
error	0.0318	0.0191	0.0117	0.0198	0.0192	0.0113

Table 7

Errors of solving hyperbolic PDE using fixed receptive field PINN and MRF-PINN

receptive field	3	5	7	9	11	MRF-PINN
error	0.0162	0.0184	0.0257	0.0248	0.0155	0.0187

Table 8

Errors of solving Navier-Stokes PDEs using fixed receptive field PINN and MRF-PINN

receptive field	3	5	7	9	11	MRF-PINN
error of u	0.0613	0.0608	0.0612	0.0608	0.0611	0.0609
error of v	0.0337	0.0451	0.0475	0.0456	0.0274	0.0249
error of w	0.0404	0.0587	0.0467	0.0463	0.0382	0.0376
error of p	0.0532	0.0615	0.0539	0.0563	0.0528	0.0522

4.2 Dimensional balance method

As mentioned in section 2.3, the dimensional balance method is used to estimate the loss weights when solving the Navier-Stokes equations. In this way, we can avoid manual tuning and reduce the solving cost of the dynamic weight method.

As shown in Fig. 15, compared with the dynamic weight method, the dimensional balance method reduces the Adam and L-BFGS resolving time of each epoch by 95% and 72%, respectively. Because the dimensional balance method only performs back-propagation once in each epoch, the dynamic weight method requires $l+1$ back-propagations (l is the number of loss functions).

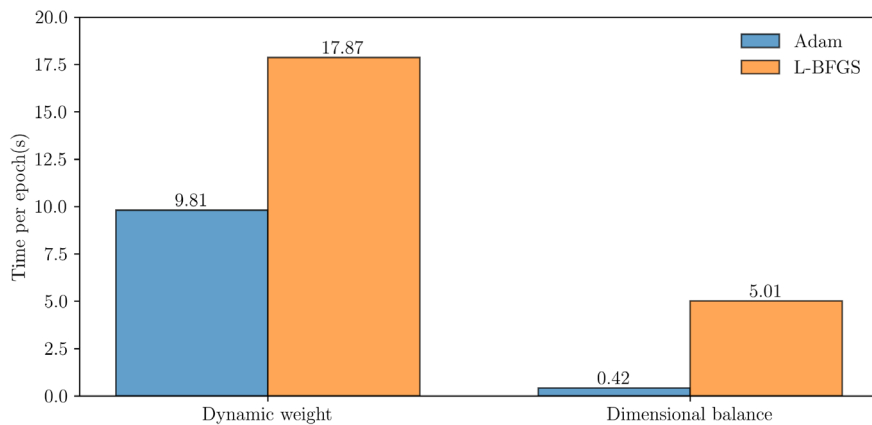


Fig. 15. Solving time of the dynamic weight method and dimensional balance method in each epoch

As shown in Fig. 16 and Fig. 17, the dimensional balance method shows better convergence than the dynamic weight estimation method. The dynamic weight estimation method collapses the solving process, while the dimensional balance method maintains a good convergence process.

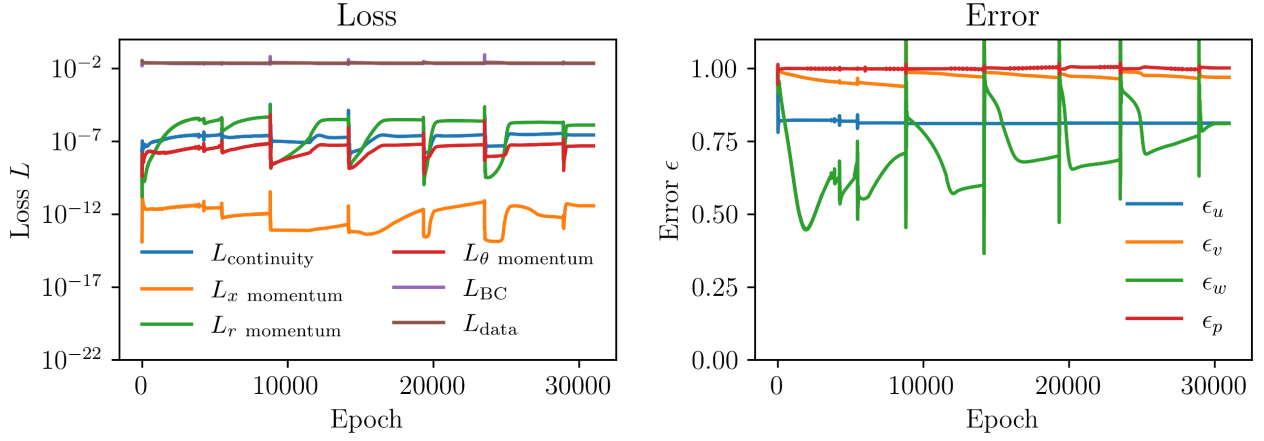


Fig. 16. Solving loss and error when using the dynamic weight method

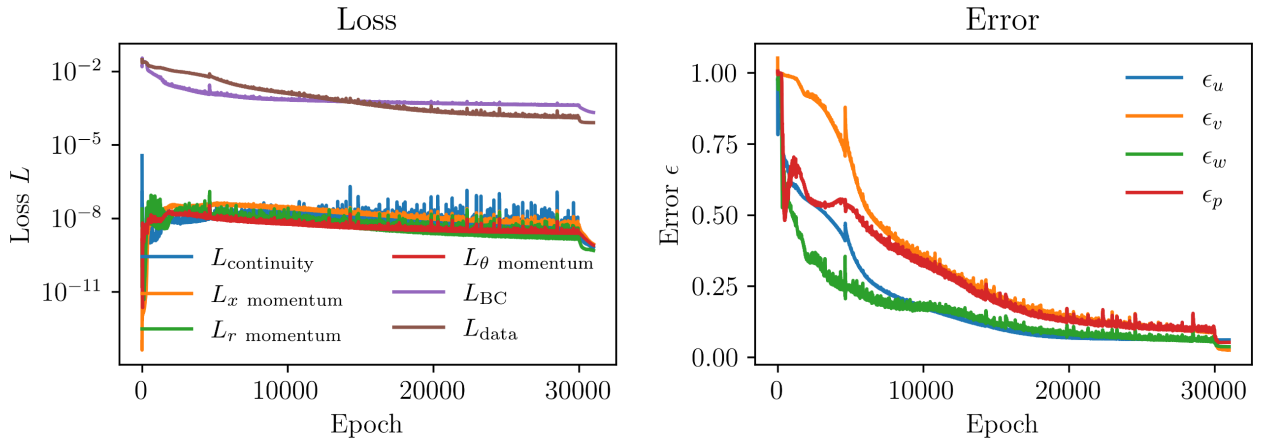


Fig. 17. Solving loss and error when using the dimensional balance method

5. Influence to MRF-PINN

5.1 Finite difference accuracy

5.1.1 Elliptic PDE

As shown in Table 9, when solving the elliptic equation, the error of the

MRF-PINN prediction result is reduced with higher differential accuracy (the 8-order difference is 3.1%, 1.6%, and 2.3% lower than the 2-order difference under different channel numbers, respectively). The prediction error of the 6-order difference is lower than that of the 8-order only when the channel number is 128. High-order finite difference can reduce the prediction error of the MRF-PINN model overall. In addition, the prediction error does not show a significant dependence on the channel number when the channel number is increased from 4 to 128.

Table 9

Elliptic PDE: influence of channel number and finite difference accuracy on prediction error and solving cost

channel number	2-order difference	4-order difference	6-order difference	8-order difference	FLOPs	Parameters
4	0.0129	0.0127	0.0127	0.0125	2.43M	4.95K
32	0.0129	0.0127	0.0127	0.0127	58.4M	281K
128	0.0129	0.0128	0.0126	0.0127	769M	4442K

5.1.2 Parabolic PDE

As shown in Table 10, when solving the parabolic equation, the prediction error of MRF-PINN is less than 0.01 under different channel numbers and finite difference accuracy. The prediction error does not always decrease as the finite difference accuracy improves. This may be due to the prediction accuracy of the parabolic equation being already very small, and the high-order finite difference has limited improvement. In addition, when the channel number is increased from 4 to 128, the prediction error and the channel number do not show obvious dependence on it.

Table 10

Parabolic PDE: influence of channel number and finite difference accuracy on prediction error and solving cost

channel number	2-order difference	4-order difference	6-order difference	8-order difference	FLOPs	Parameters
----------------	--------------------	--------------------	--------------------	--------------------	-------	------------

4	0.00758	0.00748	0.00783	0.00823	2.43M	4.95K
32	0.00769	0.00709	0.00734	0.00707	58.4M	281K
128	0.00781	0.00758	0.00787	0.00736	769M	4442K

5.1.3 Hyperbolic PDE

As shown in Table 11, the higher-order finite difference significantly suppresses the prediction error when solving the hyperbolic equation. Compared with the 2-order finite difference, the prediction errors of the 8-order difference under different channel numbers are reduced by 15%, 4.3%, and 4.5%, respectively. In addition, the higher channel number reduces the prediction error under the high-order finite difference.

Table 11

Hyperbolic PDE: influence of channel number and finite difference accuracy on prediction error and solving cost

channel number	2-order difference	4-order difference	6-order difference	8-order difference	FLOPs	Parameters
4	0.0654	0.0554	0.0609	0.0554	2.43M	4.95K
32	0.0576	0.0555	0.0554	0.0551	58.4M	281K
128	0.0577	0.0554	0.0554	0.0551	769M	4442K

5.1.4 Navier-Stokes PDEs

PIV can only measure the parallel velocity component u and v on the plane but cannot measure the vertical velocity component w and pressure p . Therefore, we infer the velocity component w and the pressure p when the velocity components u and v are known. Therefore, the prediction errors of velocity components u and v can be regarded as fitting errors, while the errors of velocity components w and pressure p can be regarded as inference errors.

As shown in Table 12 and Table 13, the fitting error of the velocity component u is not significantly affected by the finite difference accuracy and the channel number. The fitting error of the velocity component v decreases when the channel number and the finite difference accuracy increase. Since the velocity components u and v are

directly supervised by the known data, they are mainly affected by the constraint of data loss.

As shown in Table 14 and Table 15, the prediction error is generally reduced when the finite difference accuracy is improved. The low-order finite difference can actually make the inference error of w lower when the channel number of the MRF-PINN is low. Moreover, as the channel number increases, the higher-order finite difference remakes the inference error of w higher than that of the lower-order finite difference. The inference error of p is similar to the conclusion of w . More channels and the high-order finite difference can reduce the inference error effectively. Compared with 4 channels and 2-order finite difference, the inference errors of w and p with 128 channels and 8-order difference are reduced by 69% and 77%, respectively. At the same time, if we adopt the high channel number and high-order finite difference, the fitting error of the velocity components u and v does not have much influence.

Table 12

Fitting error of u

channel number	2-order difference	4-order difference	6-order difference	8-order difference	FLOPs	Parameters
4	0.133	0.132	0.133	0.133	30.9M	6.28K
32	0.133	0.134	0.134	0.134	478M	291K
128	0.134	0.134	0.134	0.135	5127M	4484K

Table 13

Fitting error of v

channel number	2-order difference	4-order difference	6-order difference	8-order difference	FLOPs	Parameters
4	0.102	0.133	0.147	0.136	30.9M	6.28K
32	0.105	0.0975	0.0963	0.094	478M	291K
128	0.105	0.0965	0.0955	0.0947	5127M	4484K

Table 14

Inference error of w

channel number	2-order difference	4-order difference	6-order difference	8-order difference	FLOPs	Parameters
4	0.295	0.361	0.313	0.375	30.9M	6.28K
32	0.0970	0.0921	0.0934	0.0948	478M	291K
128	0.0976	0.0938	0.0920	0.0927	5127M	4484K

Table 15

Inference error of p

channel number	2-order difference	4-order difference	6-order difference	8-order difference	FLOPs	Parameters
4	0.413	0.537	0.366	0.462	30.9M	6.28K
32	0.137	0.115	0.114	0.121	478M	291K
128	0.141	0.107	0.105	0.103	5127M	4484K

5.2 Mesh resolution

With traditional numerical calculation methods such as FEM and FVM, the mesh resolution will directly affect the solving error and cost. In the test of MRF-PINN, it is found that MRF-PINN can also effectively reduce the solving error under high mesh resolution. However, the FLOPs and the mesh number increase proportionally.

As shown in Table 16, Table 17, and Table 18 for solving linear PDEs, when the mesh resolution is increased from 32×64 to 128×256 (the mesh number is increased by 16 times), the FLOPs also increase by 16 times, and the prediction errors are reduced by 79%, 12%, and 66%, respectively (Except for parabolic PDE at mesh resolution 128×256).

As shown in Table 19 for solving the nonlinear Navier-Stokes PDEs, increasing the mesh resolution from 32×64 to 128×256 , the fitting errors of u and v are reduced by 55% and 74%, respectively, and the inference errors of w and p are reduced by 59% and 49%. This proves that high-resolution mesh can also suppress the solving error in MRF-PINN, but the FLOPs increase simultaneously.

Table 16

Elliptic PDE: the influence of mesh resolution on error and FLOPs

mesh resolution	32×64	64×128	128×256
error	0.0127	0.00621	0.00263
FLOPs	770M	3078M	12312M

Table 17

Parabolic PDE: the influence of mesh resolution on error and FLOPs

mesh resolution	32×64	64×128	128×256
error	0.00736	0.00645	0.0113
FLOPs	770M	3078M	12312M

Table 18

Hyperbolic PDE: the influence of mesh resolution on error and FLOPs

mesh resolution	32×64	64×128	128×256
error	0.0551	0.0326	0.0187
FLOPs	770M	3078M	12312M

Table 19

Navier-Stokes PDEs: the influence of mesh resolution on error and FLOPs

mesh resolution	32×384	64×768	128×1536
Error of u	0.135	0.0861	0.0609
Error of v	0.0947	0.0627	0.0249
Error of w	0.0927	0.0572	0.0376
Error of p	0.103	0.0726	0.0522
FLOPs	5127M	20509M	82035M

6. Summary

This paper proposes a multiple receptive field convolutional PINN(MRF-PINN) model adaptive to different equation types and mesh resolution. The MRF-PINN can solve multiple types of partial differential equations(PDEs) with low solving error and no hyperparameter tuning. In order to improve the calculation accuracy of PDE loss, we adopt the Taylor polynomial to pad the boundary of the PINN result so that it can perform high-order finite difference. In the case that the Navier-Stokes equations have many loss functions and significant difference in loss magnitudes, we first use the

dimensional balance method to estimate the loss weights.

Compared with the traditional fixed receptive field PINN, the MRF-PINN has the advantages of low manual tuning cost and low solving error. When solving Navier-Stokes equations, our proposed dimensional balance method has a shorter solving time and better convergence than the dynamic weight method. Based on MRF-PINN, we systematically study the effects of finite difference accuracy, model complexity (channel number), and mesh resolution on PINN results. Generally, similar to the traditional numerical solving method (such as FEM and FVM), the high-order finite difference is beneficial to obtaining low-error PDE solutions. Besides, the high-order finite difference does not bring about numerical instability in our tests. Higher model complexity and mesh resolution can reduce the error of the PDE solution but will simultaneously increase the FLOPs cost.

This work implies that the MRF-PINN model can adapt to different PDE types, which is expected to be a general scheme for convolutional PINN. Researchers can also use the dimensional balance method to estimate the loss weights to solve the Navier-Stokes equations. Finally, systematic numerical experiments on finite difference, model complexity, and mesh resolution fill the current weak research on convolutional PINN. Researchers are expected to achieve low-error solving results and good numerical stability at the high-order finite difference and high mesh resolution.

CRedit authorship contribution statement

Shihong Zhang: Conceptualization, Methodology, Software, Validation, Writing - Original Draft, Writing - Review & Editing. **Bosen Wang:** Supervision, Writing - Review & Editing. **Chi Zhang:** Supervision.

Declaration of competing interest

The authors declare that they have no known competing financial interests or personal relationships that could have appeared to influence the work reported in this paper.

Acknowledgements

Thanks to the National Natural Science Foundation of China (52106128) and the National Science and Technology Major Project (J2019-III-0014-0057) for their financial support.

References

- [1] H. Jasak, A. Jemcov, Z. Tukovic, OpenFOAM: A C++ Library for Complex Physics Simulations, (n.d.) 20.
- [2] E. Giner, N. Sukumar, J.E. Tarancón, F.J. Fuenmayor, An Abaqus implementation of the extended finite element method, *Engineering Fracture Mechanics*. 76 (2009) 347–368. <https://doi.org/10.1016/j.engfracmech.2008.10.015>.
- [3] S.V. Patankar, *Numerical Heat Transfer and Fluid Flow*, (n.d.) 30.
- [4] D.M. Sullivan, *Electromagnetic simulation using the FDTD method*, John Wiley & Sons.(2013).
- [5] M. Svärd, J. Nordström, Review of summation-by-parts schemes for initial – boundary-value problems, *Journal of Computational Physics*. 268 (2014) 17 – 38. <https://doi.org/10.1016/j.jcp.2014.02.031>.
- [6] E.J.F. Dickinson, H. Ekström, E. Fontes, COMSOL Multiphysics®: Finite element software for electrochemical analysis. A mini-review, *Electrochemistry Communications*. 40 (2014) 71–74. <https://doi.org/10.1016/j.elecom.2013.12.020>.
- [7] J. Droniou, Finite volume schemes for diffusion equations: Introduction to and review of modern methods, *Math. Models Methods Appl. Sci.* 24 (2014) 1575 – 1619. <https://doi.org/10.1142/S0218202514400041>.
- [8] L. Chen, Q. Kang, Y. Mu, Y.-L. He, W.-Q. Tao, A critical review of the pseudopotential multiphase lattice Boltzmann model: Methods and applications, *International Journal of Heat and Mass Transfer*. 76 (2014) 210 – 236. <https://doi.org/10.1016/j.ijheatmasstransfer.2014.04.032>.
- [9] J.J. Monaghan, Smoothed Particle Hydrodynamics and Its Diverse Applications, *Annu. Rev. Fluid Mech.* 44 (2012) 323 – 346. <https://doi.org/10.1146/annurev-fluid-120710-101220>.
- [10] G.E. Karniadakis, I.G. Kevrekidis, L. Lu, P. Perdikaris, S. Wang, L. Yang, Physics-informed machine learning, *Nat Rev Phys*. 3 (2021) 422–440. <https://doi.org/10.1038/s42254-021-00314-5>.

- [11] M. Raissi, P. Perdikaris, G.E. Karniadakis, Physics-informed neural networks: A deep learning framework for solving forward and inverse problems involving nonlinear partial differential equations, *Journal of Computational Physics*. 378 (2019) 686–707. <https://doi.org/10.1016/j.jcp.2018.10.045>.
- [12] Z. Mao, A.D. Jagtap, G.E. Karniadakis, Physics-informed neural networks for high-speed flows, *Computer Methods in Applied Mechanics and Engineering*. 360 (2020) 112789. <https://doi.org/10.1016/j.cma.2019.112789>.
- [13] X. Jin, S. Cai, H. Li, G.E. Karniadakis, NSFnets (Navier-Stokes flow nets): Physics-informed neural networks for the incompressible Navier-Stokes equations, *Journal of Computational Physics*. 426 (2021) 109951. <https://doi.org/10.1016/j.jcp.2020.109951>.
- [14] S. Cai, Z. Mao, Z. Wang, M. Yin, G.E. Karniadakis, Physics-informed neural networks (PINNs) for fluid mechanics: A review, (2021). <http://arxiv.org/abs/2105.09506> (accessed May 28, 2022).
- [15] S. Cai, Z. Wang, L. Lu, T.A. Zaki, G.E. Karniadakis, DeepM&Mnet: Inferring the electroconvection multiphysics fields based on operator approximation by neural networks, *Journal of Computational Physics*. 436 (2021) 110296. <https://doi.org/10.1016/j.jcp.2021.110296>.
- [16] Y. Zhu, N. Zabaras, P.-S. Koutsourelakis, P. Perdikaris, Physics-Constrained Deep Learning for High-dimensional Surrogate Modeling and Uncertainty Quantification without Labeled Data, *Journal of Computational Physics*. 394 (2019) 56–81. <https://doi.org/10.1016/j.jcp.2019.05.024>.
- [17] M. Chen, R. Lupoiu, C. Mao, D.-H. Huang, J. Jiang, P. Lalanne, J. Fan, Physics-augmented deep learning for high-speed electromagnetic simulation and optimization, In Review, 2021. <https://doi.org/10.21203/rs.3.rs-807786/v1>.
- [18] Z. Fang, A High-Efficient Hybrid Physics-Informed Neural Networks Based on Convolutional Neural Network, *IEEE Transactions on Neural Networks and Learning Systems*. (2021) 1–13. <https://doi.org/10.1109/TNNLS.2021.3070878>.

- [19] R. Wang, K. Kashinath, M. Mustafa, A. Albert, R. Yu, Towards Physics-informed Deep Learning for Turbulent Flow Prediction, in: Proceedings of the 26th ACM SIGKDD International Conference on Knowledge Discovery & Data Mining, ACM, Virtual Event CA USA, 2020: pp. 1457–1466. <https://doi.org/10.1145/3394486.3403198>.
- [20] S. Wang, Y. Teng, P. Perdikaris, Understanding and mitigating gradient pathologies in physics-informed neural networks, arXiv preprint, arXiv:2001.
- [21] S. Basir, I. Senocak, Physics and Equality Constrained Artificial Neural Networks: Application to Forward and Inverse Problems with Multi-fidelity Data Fusion, ArXiv:2109.14860 [Physics]. (2022). <http://arxiv.org/abs/2109.14860> (accessed March 27, 2022).
- [22] Z. Li, N. Kovachki, K. Azizzadenesheli, B. Liu, K. Bhattacharya, A. Stuart, A. Anandkumar, Fourier Neural Operator for Parametric Partial Differential Equations, ArXiv:2010.08895 [Cs, Math]. (2021). <http://arxiv.org/abs/2010.08895> (accessed April 9, 2022).
- [23] A.D. Jagtap, K. Kawaguchi, G.E. Karniadakis, Adaptive activation functions accelerate convergence in deep and physics-informed neural networks, Journal of Computational Physics. 404 (2020) 109136. <https://doi.org/10.1016/j.jcp.2019.109136>.
- [24] X. Meng, G.E. Karniadakis, A composite neural network that learns from multi-fidelity data: Application to function approximation and inverse PDE problems, Journal of Computational Physics. 401 (2020) 109020. <https://doi.org/10.1016/j.jcp.2019.109020>.
- [25] H. Gao, L. Sun, J.-X. Wang, PhyGeoNet: Physics-informed geometry-adaptive convolutional neural networks for solving parameterized steady-state PDEs on irregular domain, Journal of Computational Physics. 428 (2021) 110079. <https://doi.org/10.1016/j.jcp.2020.110079>.

[26] L. Lu, X. Meng, Z. Mao, G.E. Karniadakis, DeepXDE: A Deep Learning Library for Solving Differential Equations, *SIAM Rev.* 63 (2021) 208–228. <https://doi.org/10.1137/19M1274067>.